



## RESEARCH ARTICLE

10.1002/2015JB012324

## Time-dependent recovery of microcrack damage and seismic wave speeds in deformed limestone

## Key Points:

- Elastic wave speeds recover at room temperature after deformation
- The recovery is of several percents in the first few days after deformation
- The recovery mechanism is microcrack closure by chemically activated local stress relaxation

## Correspondence to:

N. Brantut,  
n.brantut@ucl.ac.uk

## Citation:

Brantut, N. (2015), Time-dependent recovery of microcrack damage and seismic wave speeds in deformed limestone, *J. Geophys. Res. Solid Earth*, 120, 8088–8109, doi:10.1002/2015JB012324.

Received 1 JUL 2015

Accepted 1 NOV 2015

Accepted article online 12 NOV 2015

Published online 11 DEC 2015

Nicolas Brantut<sup>1</sup>

<sup>1</sup>Rock and Ice Physics Laboratory and Seismological Laboratory, Department of Earth Sciences, University College London, London, UK

**Abstract** Limestone samples were deformed up to 5% inelastic axial strain at an effective confining pressure  $P_{\text{eff}} = 50$  MPa in the cataclastic flow regime and subsequently maintained under constant static stress conditions (either isostatic or triaxial) for extended periods of time while elastic wave speeds and permeability were continuously monitored. During deformation, both seismic wave speeds and permeability decrease with increasing strain, due to the growth of subvertical microcracks and inelastic porosity reduction. During the static hold period under water-saturated conditions, the seismic wave speeds recovered gradually, typically by around 5% (relative to their initial value) after 2 days, while permeability remained constant. The recovery in wave speed increases with increasing confining pressure but decreases with increasing applied differential stress. The recovery is markedly lower when the samples are saturated with an inert fluid as opposed to water. The evolution in wave speed is interpreted quantitatively in terms of microcrack density, which shows that the post-deformation recovery is associated with a decrease in effective microcrack length, typically of the order to 10% after 2 days. The proposed mechanism for the observed damage recovery is microcrack closure due to a combination of backsliding on wing cracks driven by time-dependent friction and closure due to pressure solution at contacts between propping particles or asperities and microcrack walls. The recovery rates observed in the experiments, and the proposed underlying mechanisms, are compatible with seismological observations of seismic wave speed recovery along faults following earthquakes.

## 1. Introduction

In the Earth's upper crust, rocks accommodate deformation by fracturing and faulting. Fracturing occurs over a very wide range of scales, from a few micrometers up to tens to hundreds of kilometers [Scholz, 2002]. Microfractures play a key role in a number of physical properties of rocks: they provide pathways for fluid flow; they introduce an additional compliance and anisotropy, and their growth and interactions lead to macroscopic failure [e.g., Paterson and Wong, 2005]. Pervasive microcrack networks are commonly found in rocks surrounding major faults, where they form the so-called "damage zones," generated during the faulting process and due to dynamic loading during earthquakes propagation along seismogenic faults [e.g., Faulkner et al., 2010]. Freshly damaged rocks have higher permeability, lower elastic moduli, and hence lower elastic wave speeds than their intact counterparts [e.g., Faulkner et al., 2006; Mitchell and Faulkner, 2008; Rempe et al., 2013], which has an impact on the stress state on the fault core and also on the dynamics of earthquake propagation [e.g., Huang et al., 2014]. However, the long-term evolution of damaged rocks and their physical properties remains currently largely unconstrained: over time, microcracks are expected to close, heal, and become sealed by new phases. The timescales associated with these recovery processes control how quickly damaged rocks regain strength and stiffness and drive fluid flow around faults.

Seismological observations have established that seismic wave speeds around active faults generally drop during earthquakes, but recover in the postseismic period, consistent with a sequence of damage generation during rupture followed by postseismic damage "healing" and/or stress relaxation [e.g., Li et al., 2003; Schaff and Beroza, 2004; Li et al., 2006; Brenguier et al., 2008; Froment et al., 2014]. Despite the general qualitative agreement between most seismological observations, the amplitude and timescale of the postseismic elastic wave speed recovery near faults, and thus the associated mechanism, remain only loosely constrained, with typical recoveries in wave speeds ranging from 0.01% to a few percent over periods from a few days to a few years.

©2015. The Authors.

This is an open access article under the terms of the Creative Commons Attribution License, which permits use, distribution and reproduction in any medium, provided the original work is properly cited.

The recovery processes responsible for the inferred postseismic changes in wave speeds around faults can be divided into two classes: (1) recovery by microcrack *closure*, for instance, due to effective stress relaxation, and (2) recovery by microcrack *healing* or *sealing*, driven by chemical phenomena. In both cases, one of the most prominent factors that is expected to influence the long-term evolution of microcrack damage under upper crustal conditions is the presence of water. Water modifies the effective stress state and the effective elastic properties of rocks [e.g., Jaeger *et al.*, 2007]. Water is also chemically active and allows dissolution, precipitation, and transport of materials within pores and cracks, and hence promotes healing and sealing of microcracks through diffusional processes [Smith and Evans, 1984; Hickman and Evans, 1987; Brantley *et al.*, 1990; Brantley, 1992; Tenthorey and Fitz Gerald, 2006], and dissolution-precipitation processes [e.g., Rutter, 1976; Hickman and Evans, 1992; Gratier *et al.*, 2013; Richard *et al.*, 2015]. Dissolution and precipitation processes also contribute to time-dependent creep and hence they can promote time-dependent closure of microcracks by local stress relaxation [e.g., Beeler and Hickman, 2004]. A number of studies have explored the effect of microcrack closure, healing and sealing on macroscopic rock properties, showing time-dependent restrengthening [Karner *et al.*, 1997; Nakatani and Scholz, 2004; Tenthorey *et al.*, 2003; Tenthorey and Fitz Gerald, 2006] and permeability reduction [Brantley *et al.*, 1990; Tenthorey *et al.*, 1998; Morrow *et al.*, 2001; Tenthorey *et al.*, 2003] under hydrothermal conditions. However, the effect of time-dependent closure and healing on elastic properties remains poorly studied. An early work of Schubnel *et al.* [2005] showed elastic wave speed recovery during stress relaxation in fluid saturated carbonates. Similarly, recent experiments on water-saturated halite gouges [Kaproth and Marone, 2014] showed that seismic wave velocities increase during post shear stress relaxation episodes, in correlation with time-dependent compaction of the gouge. However, the stress relaxation methodology does not provide a clear way to separate chemical effects (e.g., diffusional crack healing or precipitation sealing) and purely elastic effects (i.e., crack closure due to the gradual decrease in applied stresses). Hence, our understanding of the effect of microcrack closure and healing on seismic wave speeds in rocks remains mostly phenomenological.

The goal of this paper is therefore to explore systematically the influence of deformation, stress state, and fluid type on the “healing” behavior of rocks. The rock type used here was a porous carbonate rock, chosen because (1) carbonates are a major rock type present along a large number of fault zones and (2) the dissolution and precipitation rates of calcite in water are relatively fast at low temperature, which allows to study these chemical processes over practicable laboratory timescales at room temperature. Triaxial deformation tests were conducted at elevated confining pressure, in the cataclastic flow regime, in order to generate a homogeneous, anisotropic microcrack network in the rock. Subsequently, the deformed samples were unloaded and kept under constant stress conditions for extended periods of time, while permeability and elastic wave speeds were continuously monitored.

The experimental methodology is described in section 2, and the results from the triaxial deformation experiments are reported in section 3. Section 4 presents the results from the static hold tests, in which the influence of stress state (confining pressure and differential stress), deformation cycles, and fluid type (water or decane, a chemically inert fluid) was tested. The resulting microstructures are described in section 5. In section 6, the elastic wave speed data are interpreted in terms of microcrack density, and quantitative estimates of microcrack recovery rates under the various experimental conditions tested are documented. Finally, in section 7 the potential mechanisms responsible for the observed recovery are examined, and the implications for fault mechanics are discussed.

## 2. Experimental Methods

The rock selected for this study was a porous limestone from the south coast of England named Pond free-stone Purbeck limestone, the same material as the one used by Brantut *et al.* [2014b] to study brittle creep. This limestone is a grainstone composed of 80% calcite and 20% quartz; its average porosity is 13.8% and its nominal permeability is around  $2 \times 10^{-16} \text{ m}^2$ . Cylindrical samples of 40 mm in diameter and 100 mm in length were cored perpendicular to the sedimentary bedding. The samples were dried at 60°C for at least 1 week prior to testing. Each sample was inserted in a viton jacket and placed in the pressure vessel of the triaxial deformation apparatus at University College London (see description in Eccles *et al.* [2005]). An oil confining pressure of 20 MPa was applied, and the sample was then saturated with a pore fluid (distilled water or decane). When saturation was complete, the pore fluid pressure was increased up to 10 MPa. The confining pressure was subsequently stepped up to 60 MPa, and the sample was left to stabilize for 3 to 4 h in order to allow the confining and fluid pressures to stabilize. This stabilization time was not sufficiently long for the

**Table 1.** Summary of the Samples Tested and Experimental Conditions

Sample	Axial Strain (%)	Duration (h)	$P_{\text{eff}}$ (MPa)	$Q$ (MPa)	$P_m$ (MPa)	$V_p(90^\circ)$	Recovery at 40 h (%)	Notes
PL-29	5.17	64.7	50	0	50		4.3	
PL-28	5.05	60.6	80	0	80		5.6	
PL-30	5.17	87.1	20	0	20		3.1	
PL-32	2.09	64.3	50	0	50		3.0	first cycle
–	4.92	47.2	50	0	50		3.6	second cycle
PL-33	5.41	21.8	50	79	76		–	
PL-34	4.96	195.9	60	0	60		4.9	
PL-35	4.93	44.7	70	0	70		5.0	
PL-36	5.18	138.1	50	30	60		4.1	
PL-37	5.33	44.5	50	60	70		4.1	
PL-38	5.44	141.9	50	90	80		3.8	
PL-39	5.32	141.6	50	60	70		4.0	
PL-40	0.49	71.3	50	0	50		1.0	first cycle
–	1.21	71.2	50	0	50		2.2	second cycle
–	2.08	69.9	50	0	50		2.7	third cycle
–	3.03	70.8	50	0	50		3.2	fourth cycle
–	4.12	69.8	50	0	50		3.4	fifth cycle
–	5.02	138.3	50	0	50		2.9	sixth cycle
PL-42	4.70	89.1	50	0	50		1.5	decane

chemical composition of the fluid to fully equilibrate with the rock, and the pore fluid (in the case of water) remained undersaturated with respect to calcite at the time deformation was started.

Triaxial deformation tests were performed at a constant axial strain rate of  $10^{-5} \text{ s}^{-1}$  and at an effective confining pressure of  $P_{\text{eff}} = 50 \text{ MPa}$ . Sample shortening was calculated from an external measurement of the ram displacement (with a pair of Linear Variable Differential Transformers, LVDTs), corrected for the elastic distortion of the piston assembly. Axial load was measured with an external 150 ton load cell. After deformation, the axial load on the sample was removed (so that the imposed differential stress is reduced to zero) and the confining and pore pressures were kept constant for extended hold times (isostatic hold tests). In several tests, non-isostatic conditions were maintained during the hold period (triaxial hold tests). In those cases, the unloading was partial and the axial load was subsequently kept constant using a servocontrolled actuator.

The pore pressure was imposed with a fast-acting servocontrolled intensifier and measured with two independent transducers located on each side of the sample (upstream and downstream). During the tests, the upstream pore pressure was oscillated around the mean value of 10 MPa at a period of 15 s and an amplitude of  $\pm 0.2 \text{ MPa}$ . The downstream pressure was monitored, and the phase shift and amplitude ratio between the upstream and downstream pore pressure signals was used to determine the permeability of the sample [Fischer and Paterson, 1992; Bernabé et al., 2006]. Specifically, the discrete Fourier transform of a moving window of 10 cycles was computed for each signal, and the phase shift and amplitude ratio were computed by spectral division. The permeability was then inverted using the method of Bernabé et al. [2006]. The relative weight of the amplitude ratio and phase shift data was adjusted between 0.5 up to 0.8 in order to obtain consistent results. The storage capacity could not be inverted within reasonable error bounds due to the large uncertainty of the method for this particular combination of parameters [Bernabé et al., 2006].

The pore volume change in the sample was monitored by tracking the volume in the pore fluid intensifier with an LVDT. Because of thermal effects and a long-term drift in this measurement, the pore volume change could not be measured accurately during the extended hold periods of the tests and hence only its evolution during the deformation periods is presented here.

The jacketed samples were equipped with an array of 16 piezoelectric transducers connected to high-frequency preamplifiers (40 dB) and a 50 MHz digital oscilloscope. The transducers were repeatedly and



**Figure 1.** Photograph of an intact sample and a sample deformed up to 5% axial strain at  $P_{\text{eff}} = 50$  MPa.

technique [see *Brantut et al.*, 2011, 2014b]. The overall accuracy of the method was improved by resampling the waveforms at 100 MHz using cubic splines, so that the relative accuracy of the wave speed measurements was of the order of 0.1%.

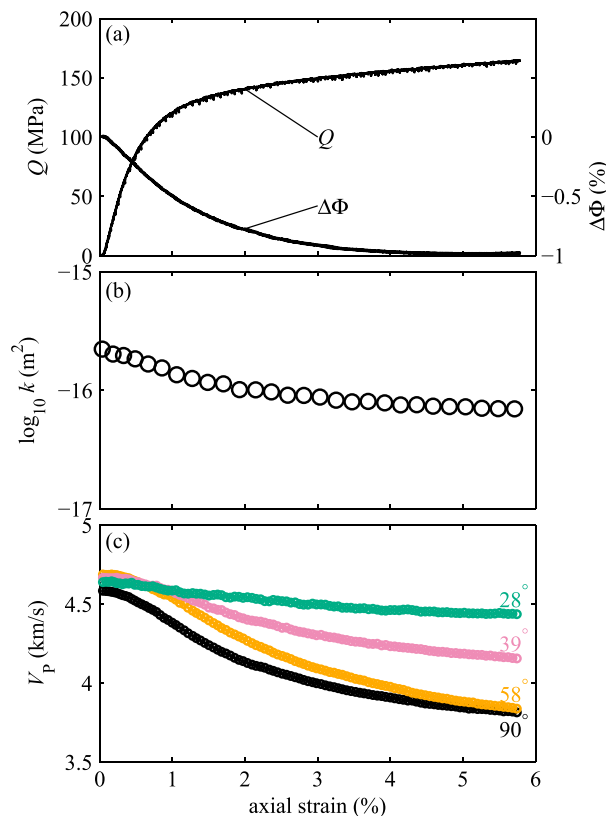


**Figure 2.** Mechanical behavior of Purbeck limestone during deformation at constant strain rate  $10^{-5} \text{ s}^{-1}$  and  $P_{\text{eff}} = 50$  MPa: (a) Differential stress ( $Q$ ) and porosity change  $\Delta\Phi$ , (b) permeability, and (c)  $P$  wave speed evolution as a function of axial strain.

sequentially used as sources and receivers to monitor the evolution of elastic wave speeds throughout the tests. The array geometry (same as the one used in *Brantut et al.* [2014a, 2014b]) allowed to measure the  $P$  wave speed along four different angles with respect to the compression axis ( $90^\circ$ ,  $58^\circ$ ,  $39^\circ$ , and  $28^\circ$ ) as well as the  $S_h$  wave speed along the horizontal ( $90^\circ$ ) direction. At regular time intervals during the tests, a 250 V, 1 MHz pulse was sent sequentially to each transducer while recording the resulting waveforms from the remaining sensors. Each shot was repeated 6 times, and the resulting waveforms were stacked to improve the signal-to-noise ratio. A reference “master” survey, usually the first one in the series, was selected and arrival times were picked manually on each waveform. Then, for each source-receiver pair, the relative change in arrival time was subsequently measured automatically by using a cross-correlation

A summary of the test conditions is given in Table 1. Most samples were deformed until around 5% inelastic axial strain (measured after unloading), and selected samples were also deformed cyclically with around 1% axial strain at each step. Hold times ranged from 22 h up to 196 h.

### 3. Triaxial Deformation Experiments

At  $P_{\text{eff}} = 50$  MPa, the behavior of Purbeck limestone is ductile [*Brantut et al.*, 2014b], and a photograph of a sample deformed under these conditions is shown in Figure 1: at the sample scale no strain localization feature is visible, but the sample shows evidence of barrelling. The mechanical behavior, shown in Figure 2a, exhibits strain hardening and the pore volume shows an overall compactant behavior. At around 5% axial strain, the pore volume change reaches a minimum and tends to increase, indicating net dilatancy. This behavior is typical of porous limestone deformed in the ductile regime and implies that dilatant cracking becomes dominant over porosity reduction after some given strain threshold [see *Wong and Baud*, 2012].

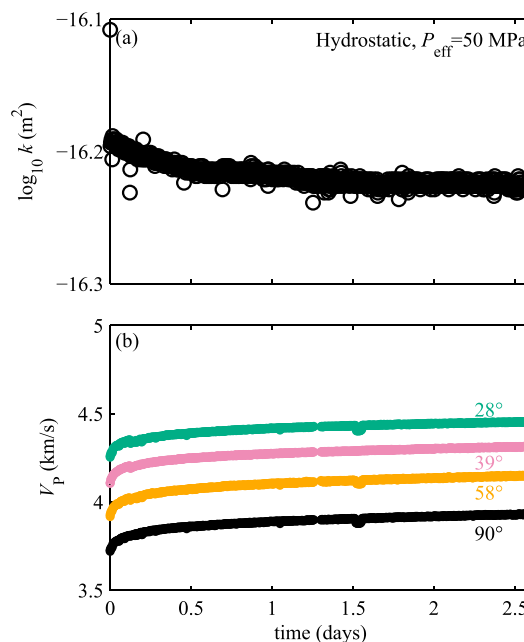


**Figure 3.** Healing behavior under isostatic conditions at  $P_{\text{eff}} = 50$  MPa: (a) permeability and (b)  $P$  wave speed as a function of time.

The permeability decreases monotonically throughout deformation, by around a factor of 3 at 5.7% strain (Figure 2b). This behavior is qualitatively similar to that in porous sandstone in the ductile regime [e.g., Zhu and Wong, 1997].

The  $P$  wave speeds all decrease with increasing strain (Figure 2c). The horizontal  $P$  wave speed (i.e., measured at  $90^\circ$  from the compression axis) decreases by 17.4%, from an initial value of 4.6 km/s down to 3.8 km/s at 5.7% strain, while the  $P$  wave speed measured at  $28^\circ$  from the compression axis decreases only by 7.5%, down to 4.4 km/s (i.e., a 7.5% drop). At any given strain, the  $P$  wave speed decrease is overall smaller along the paths at angles closer to the compression axis. This is indicative of the development of elastic anisotropy, consistent with the preferential growth of subvertical microcracks [e.g., Schubnel et al., 2005; Brantut et al., 2014b].

Taken together, these observations are characteristics of the ductile, cataclastic flow regime in porous limestone [e.g., Wong and Baud, 2012] and indicate that the material accommodates deformation by diffuse, mostly subvertical microcrack.

#### 4. Recovery Under Static Stress Conditions

The typical behavior of the deformed rock during the hold period is shown in Figure 3, which corresponds to the reference case of recovery under isostatic conditions at  $P_{\text{eff}} = 50$  MPa. The permeability (Figure 3a) remains essentially constant throughout the hold period; the observed minute decrease (here of around 7%) is not reproducible and most experiments did not show any consistent substantial variations in permeability during that stage. By contrast, the  $P$  wave speed in all the measured orientations increased gradually throughout the hold period. Immediately after deformation and unloading, the increase is relatively fast and subsequently slows down over time: for instance, the horizontal  $P$  wave speed increased from 3.72 km/s up to 3.86 km/s in the first 12 h of the healing period and reaches 3.93 km/s after 60 h. Except for the initial offsets between the measurements (partly arising from the error in the manual picking of arrival times, required to measure the absolute wave speeds), no significant difference is observed between the recovery in  $P$  wave speed along subvertical orientations and that observed along subhorizontal orientations.

The evolution of the recovery in  $P$  wave speed as a function of time under isostatic conditions for  $P_{\text{eff}}$  ranging from 20 to 80 MPa is shown in Figure 4. To clarify the comparison between tests conducted under different conditions, the recovery in  $P$  wave speed is shown here as the ratio  $(V_p - V_p^0)/V_p^{\text{ref}}$ , where  $V_p^0$  is the  $P$  wave speed measured at the beginning of the healing period, and  $V_p^{\text{ref}}$  is the reference  $P$  wave speed of the intact rock before deformation, taken as 4.6 km/s. For any given effective pressure, the velocity increase is of similar magnitude for all orientations; and is of the order of 4% at  $P_{\text{eff}} = 20$  MPa, increasing up to more than 6% at  $P_{\text{eff}} = 80$  MPa after a hold period of  $2 \times 10^5$  s (55 h). The  $P$  wave speeds measured along subvertical paths are relatively less influenced by confining pressure than those measured along subhorizontal paths: at  $2 \times 10^5$  s (55 h), the recovery along the  $28^\circ$  path ranges from 3.8% at  $P_{\text{eff}} = 20$  MPa to 5.6% at  $P_{\text{eff}} = 80$  MPa, while along the horizontal ( $90^\circ$ ) path it ranges from 3.4% at  $P_{\text{eff}} = 20$  MPa to 6.0% at  $P_{\text{eff}} = 80$  MPa. When renormalized by the actual  $P$  wave velocity drop  $(V_p^{\text{ref}} - V_p^0)$  that occurred during deformation, the resulting relative recovery in  $P$  wave speed after  $2 \times 10^5$  s ranges from around 10% at  $P_{\text{eff}} = 20$  MPa up to more than 40% at  $P_{\text{eff}} = 80$  MPa, with a relative recovery  $(V_p - V_p^0)/(V_p^{\text{ref}} - V_p^0) = 24.1\%$  at the reference  $P_{\text{eff}} = 50$  MPa.

The effect of differential stress was investigated by maintaining a constant load on the sample throughout the hold period (triaxial hold tests). In order to make meaningful comparisons between the isostatic

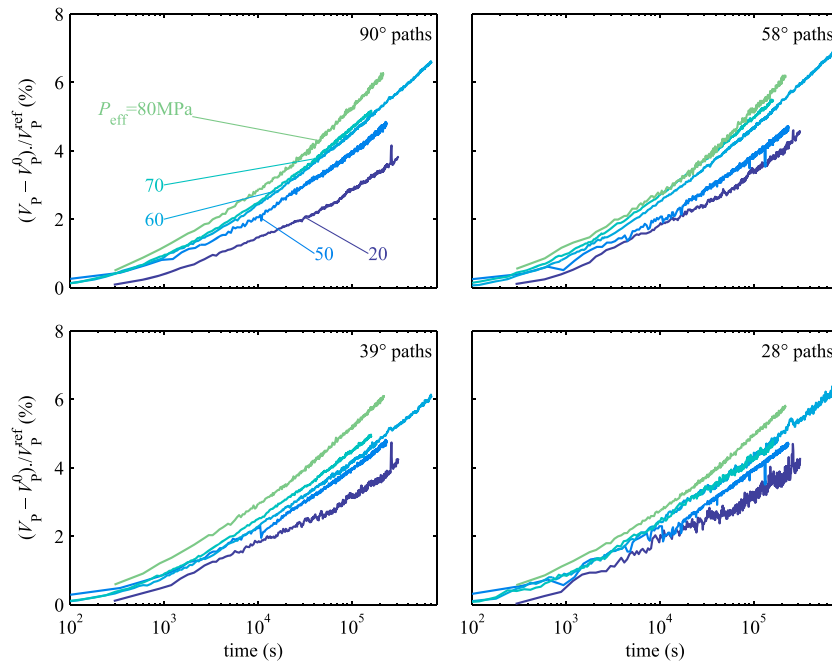


**Figure 4.** Recovery in *P* wave speed along the four available orientations with respect to the compression axis during healing tests performed at  $P_{eff} = 20, 50, 60, 70,$  and  $80$  MPa ( $Q = 0$ ). The recovery is measured as the difference between the current  $V_p$  and the initial measure  $V_p^0$  at the start of the hold period, normalized by the reference “intact”  $V_p = 4.6$  km/s.

(described above) and triaxial hold tests, for the latter the effective confining pressure and differential stresses were chosen to reproduce the same effective mean stresses of 50, 60, 70, and 90 MPa as those investigated in the isostatic experiments (where the effective mean stress is simply equal to the effective confining pressure). Therefore, the effective confining pressure was kept at  $P_{eff} = 50$  MPa and the applied differential stress was set to  $Q = 30, 60,$  or  $90$  MPa in order to produce effective mean stresses  $P_m = P_{eff} + Q/3$  of 60, 70, or 80 MPa, respectively. Under these conditions no significant axial creep deformation was recorded. The results are shown in Figure 5, where the relative recovery in *P* wave speed along the horizontal paths is plotted as a function of hold time for each pair of experiments performed at the same  $P_m$  but for different  $P_{eff}$  and  $Q$ . For any given effective mean stress, the application of a differential stress generally induces a slower *P* wave speed recovery during the first  $10^4$  s (around 2.8 h) of the hold period, while the subsequent recovery rate parallels the one measured under isostatic conditions. The time interval during which the *P* wave speed recovery rate remains lower at  $Q > 0$  than at  $Q = 0$  increases with increasing  $Q$ . As a result, for any given hold time the relative recovery is systematically lower when a differential stress is applied than under purely isostatic

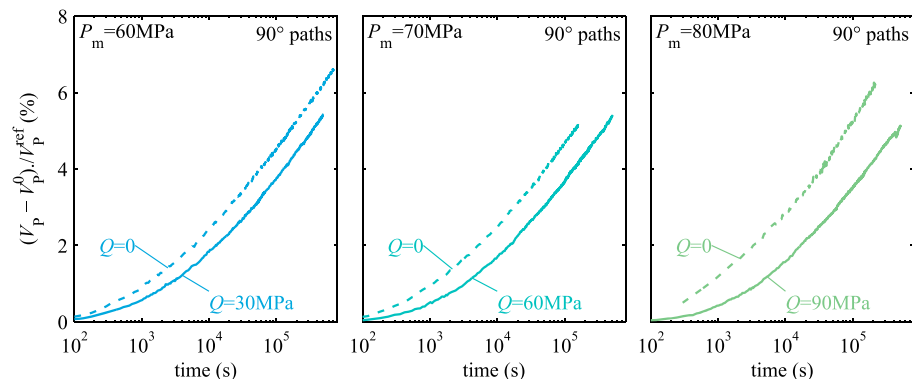


**Figure 5.** Recovery in *P* wave speed along the horizontal paths as a function of hold time, for isostatic and triaxial conditions.

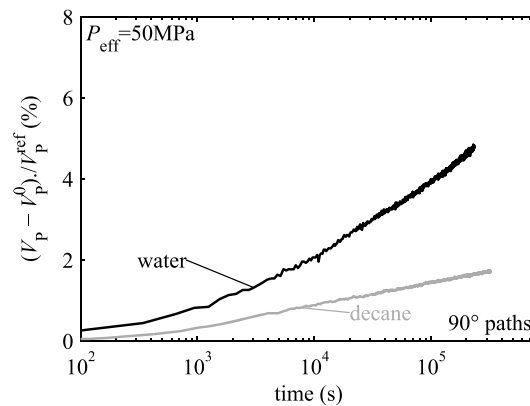


**Figure 6.** Recovery in  $P$  wave speed along the horizontal paths as a function of hold time under isostatic  $P_{\text{eff}} = 50$  MPa conditions, for water-saturated and decane-saturated samples.

cases, but the relative recovery is much lower with decane than with water; after  $2 \times 10^5$  s, the recovery is only of 1.6% with decane whereas it is 4.6% with water.

The above observations of  $P$  wave speed recovery under different conditions are summarized in Figure 7, which shows the relative recovery in  $P$  wave speed (along  $90^\circ$  paths) after  $1.44 \times 10^5$  s (40 h) as a function of effective mean stress. This plot indicates that the relative  $P$  wave speed recovery increases with increasing isostatic stress, but decreases with increasing differential stress. The effect of water is clearly highlighted by the markedly lower recovery observed when decane is used instead of water as the pore fluid.

In order to examine the effect of initial deformation on the recovery rate, a sample was deformed sequentially in six steps, each consisting of a cycle of loading at a constant strain rate of  $10^{-5} \text{ s}^{-1}$  to a fixed strain, and then unloading at the same strain rate, followed by an isostatic hold period of  $2.6 \times 10^5$  s (3 days). After the last deformation cycle, the hold period was extended to  $5.2 \times 10^5$  s (6 days). The resulting recovery behavior is shown in Figure 8, where the relative change in  $P$  wave speed from the reference intact value is plotted as a function of time for the successive hold periods following the deformation cycles. The first cycle produced a finite inelastic (irrecoverable) strain of 0.5%; the recovery during the hold period is overall quite limited and occurs relatively rapidly in the first few hours after deformation, while no significant long-term recovery trend remains visible after 3 days. In all the subsequent hold periods following each cycle, from 1.2 to 5.0% inelastic strain, the trend in  $P$  wave speed recovery is qualitatively similar to that observed in all the samples deformed

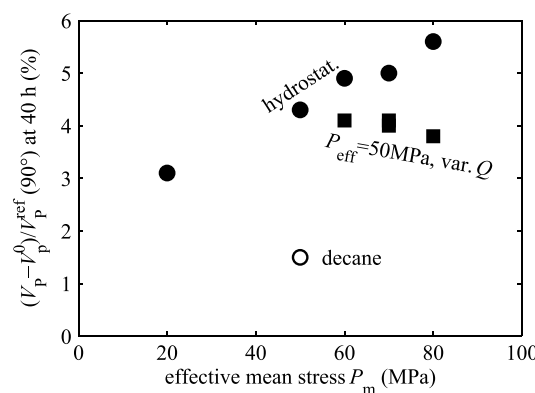


**Figure 7.** Relative recovery in  $P$  wave speed along horizontal paths after 40 h of hold time as a function of the effective mean stress  $P_m = P_{\text{eff}} + Q/3$ . Filled circles correspond to isostatic experiments, squares correspond to triaxial recovery experiments performed at  $P_{\text{eff}} = 50$  MPa and  $Q = 30, 60,$  and  $90$  MPa, and the open circle correspond to the test performed at  $P_{\text{eff}} = 50$  MPa using decane as a pore fluid.

conditions. For instance, at  $P_m = 80$  MPa, the horizontal  $P$  wave speed has recovered by about 6.1% under isostatic conditions but only by 4.2% under triaxial conditions ( $P_{\text{eff}} = 50$  MPa,  $Q = 90$  MPa) after a hold period of  $2 \times 10^5$  s.

The influence of pore fluid chemistry on recovery was also tested during an experiment in which decane was used as the pore fluid. Decane has the same viscosity as water at room temperature, but has negligible chemical interactions with calcite and quartz [e.g., Zhang and Spiers, 2005]. The resulting relative  $P$  wave speed recovery is plotted in Figure 6, which compares results from the tests performed under water- and decane-saturated conditions at  $P_{\text{eff}} = 50$  MPa. The  $P$  wave speed recovers in both

directly to around 5% strain: a rapid recovery in the first few hours after deformation is followed by a continuing, slower long-term recovery. Remarkably, from 2.1% strain and above, the recovery after 3 days between each step is essentially total: the  $P$  wave speed tends to increase back to its value prior to deformation, at the end of the previous hold period. The measurement method uses new manual  $P$  wave picking at the beginning of each hold period; hence, the absolute value of the  $P$  wave speed is likely slightly offset between each period, which is a probable explanation for the variability in  $P$  wave speed drop after each deformation step.

The progressive relative recovery following each deformation step is plotted in Figure 9; for clarity, only the  $P$  wave speed recovery measured along horizontal paths is shown. Overall, the  $P$  wave speed tends to increase faster with increasing prior deformation of the sample.

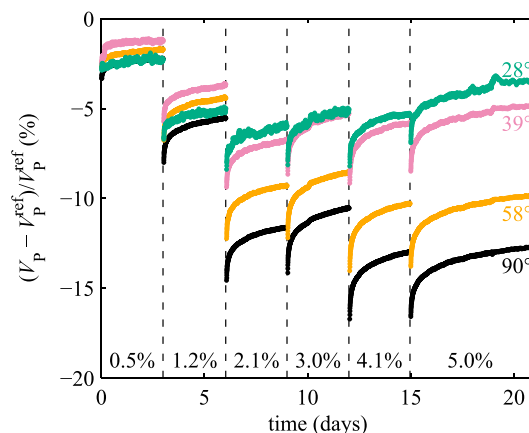


**Figure 8.** Relative recovery in  $P$  wave speed, along four propagation angles, as a function of time, for a sequential deformation experiment. The sample was loaded, deformed, and unloaded at a constant strain rate of  $10^{-5} \text{ s}^{-1}$  between each hold period. The axial strain (measured after unloading) at the end of each deformation step is marked as a percentage on the plot. Note that the change in  $P$  wave speed is computed here using the initial, intact value as a reference.

Figures 10b–10f show representative microstructures, observed in sample PL-34 which was deformed at  $P_{\text{eff}} = 50 \text{ MPa}$  to 5% strain and subsequently underwent an isostatic hold period of 196 h at  $P_{\text{eff}} = 60 \text{ MPa}$ . A large number of subvertical microcracks is observed throughout the sample. These cracks are homogeneously distributed throughout the rock and are of two distinct types: intragranular, thin, and straight in the large calcite crystals forming the cement (Figure 10c), and intergranular, thick, and tortuous, within the peloids (Figure 10b). Additional optical observations show that the large crystal of calcite cement are extensively twinned, with dense arrays of very thin lamellae. The calcite cement is highly fractured, and the fractures are propped open by micron- and submicron-sized grain fragments detached from the peloids' rims (Figures 10d and 10f). Wing cracks are also widely observed within the cement (Figure 10c). Some scattered evidence for pore collapse can also be observed (Figure 10b), but the initial microstructure is mostly microporous and pore collapse is hence not a commonly observed deformation feature.

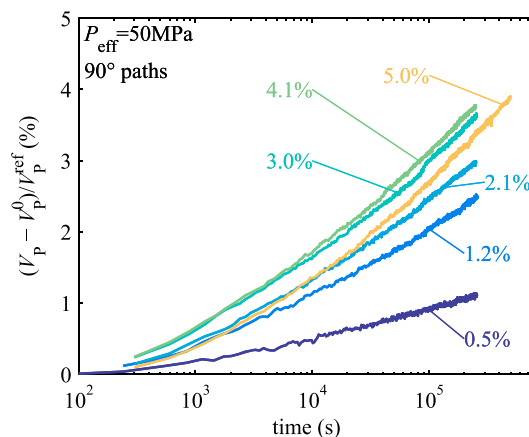


**Figure 9.** Relative recovery in  $P$  wave speed along horizontal paths as a function of hold time under isostatic  $P_{\text{eff}} = 50 \text{ MPa}$  conditions, for a sample deformed sequentially up to 0.5, 1.2, 2.1, 3.0, 4.1, and 5.0% axial strain.

For all steps beyond 2.1% strain, the  $P$  wave speed recovery rate is similar and the recovery ranges from 3 to 4% after  $2 \times 10^5 \text{ s}$ .

### 5. Microstructural Observations

Thin sections were prepared along a plane parallel to the compression axis from a selected subset of samples. Observations were performed under both optical and scanning electron microscopy (SEM). The initial microstructure of the rock consists of rounded peloids of diameters ranging from several tens to hundreds of microns, formed by a very fine-grained, microporous calcite aggregate; the peloids are cemented by large calcite single crystals (Figure 10a) [see Brantut et al., 2014b]. The calcite crystals forming the cement are mostly free of preexisting twins.

All the samples, including the one deformed and statically held under decane-saturated conditions, exhibited very similar microstructures.

While deformation features are observed throughout the samples, direct observations of microcrack healing or sealing features remain elusive. Figure 10e shows the presence of a bridge across a thin microcrack, but such features are relatively scarce (or hard to detect). Due to the limited spatial resolution of the SEM, the structural details within the fractured micrograined peloids cannot be observed (Figure 10f). Moreover, the necessary release of effective pressure to ambient conditions at the end of the experiments is also likely to have disturbed and potentially reopened any healed or sealed microcracks.

Taken together, the microstructural observations indicate that deformation is mostly accommodated by distributed subvertical microcracks, but that direct evidence of healing or sealing processes is very difficult to identify: the recovered structures are essentially indistinguishable from the deformed structures.

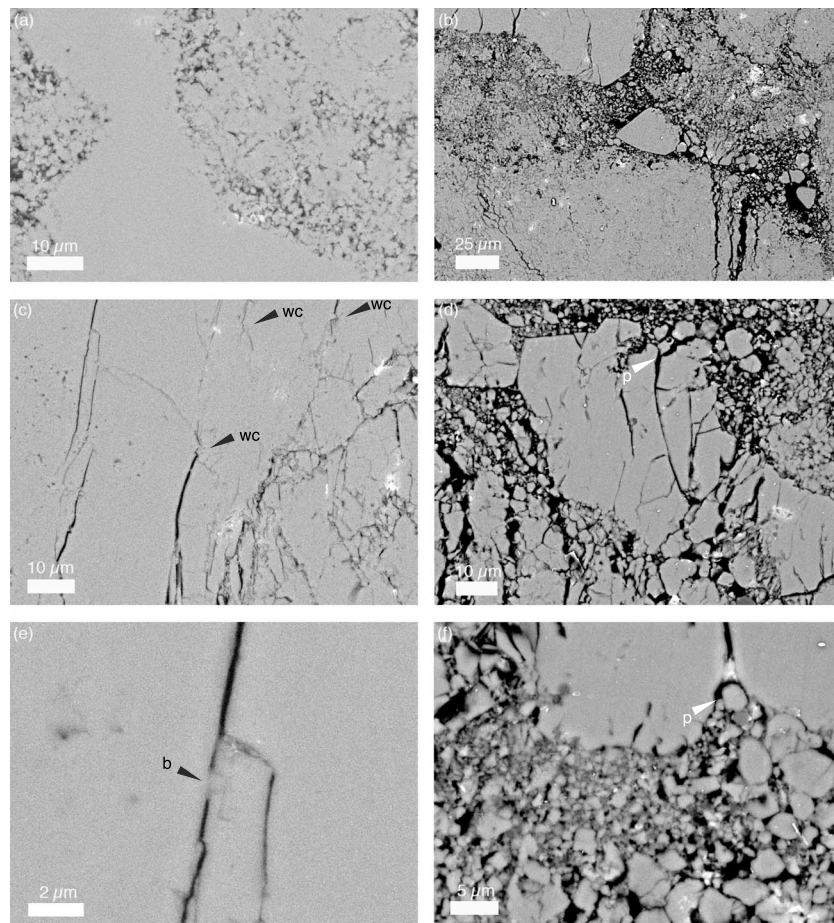


**Figure 10.** Backscattered electron scanning electron microscope photographs of Purbeck limestone. (a) Intact material prior to deformation. (b–f) Material deformed at  $P_{eff} = 50$  MPa to 5% strain and subsequently held at  $P_{eff} = 60$  MPa for 196 h (sample PL-34, see Table 1). The compression axis is vertical in all the photographs. The labels are as follows: wc, wing crack; b, bridge; and p, prop.

## 6. Estimation of Microcrack Recovery During Healing

### 6.1. Inversion of Crack Densities

The observations of elastic wave speed changes during deformation and recovery can be rationalized by quantifying the changes in microcrack density throughout the experiments. A number of micromechanical models exist to compute the effect of microcracks on averaged, effective elastic properties of porous and cracked rocks [e.g., *Salganik, 1973; Budiansky and O'Connell, 1976; Zimmerman, 1991; Kachanov, 1993*], each of them having their own advantages and limitations [see *Guéguen and Kachanov, 2011*]. Since the rock used in this study was a cracked, porous limestone, a model that included both spherical pores and thin (penny shaped) cracks was deemed appropriate and developed using the noninteraction approximation [*Kachanov, 1993; Sayers and Kachanov, 1995; Shafiro and Kachanov, 1997; Fortin et al., 2007*]. The choice of an effective medium model based on noninteracting cracks and pores is a strong simplification of the actual, complex microstructure of the samples. Therefore, this approach introduces some uncertainty in the determination and in the physical interpretation of the crack density parameters. However, such a simple approach, with a very limited number of free parameters, provides a useful first-order estimate of the relative changes in crack density during deformation and recovery, in absence of any other quantitative alternatives.

In this model, the elastic compliance of a homogeneous, elastic medium containing noninteracting microcracks and pores is written as follows [*Shafiro and Kachanov, 1997*] (see Appendix A1):

$$S_{ijkl} = S_{ijkl}^0 + \Delta S_{ijkl}^p + \Delta S_{ijkl}^c, \quad (1)$$

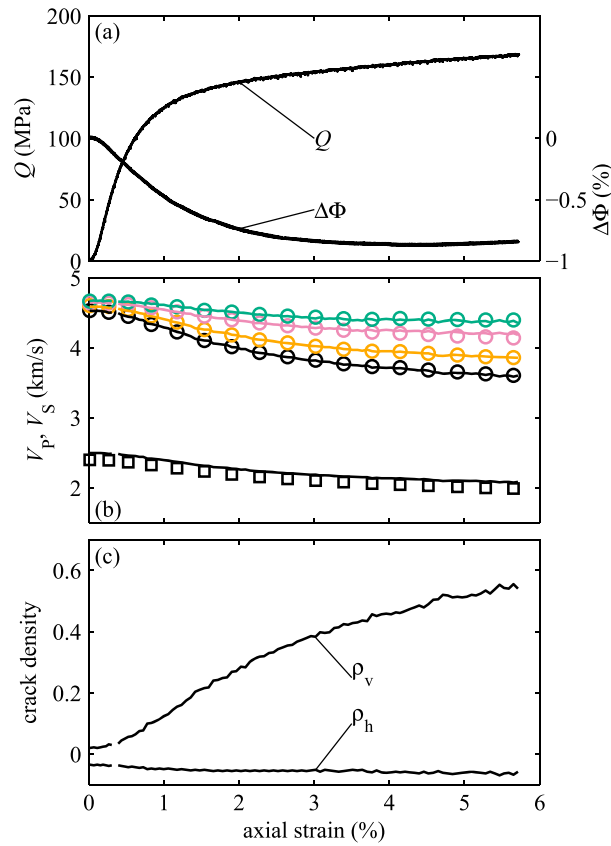


**Figure 11.** Evolution of stress, (a) pore volume change, (b) elastic wave speeds, and (c) crack density during deformation at  $P_{\text{eff}} = 50$  MPa. The crack densities  $\rho_h$  and  $\rho_v$  are defined in equations (2) and (3), respectively. Measured  $P$  wave speeds are displayed as open circles and  $S$  wave speed is shown as open squares. Modeled wave speeds are shown as continuous lines. Black, yellow, purple, and green symbols and lines correspond to  $90^\circ$  (horizontal),  $58^\circ$ ,  $39^\circ$ , and  $28^\circ$  paths, respectively.

However, in practice, the general formulation can be greatly simplified by making assumptions about the symmetry of the crack orientation distribution. Based on the symmetry of the loading configuration, we expect a transversely isotropic orientation distribution [e.g., *Sayers and Kachanov*, 1995], for which only five parameters are required. In order to further reduce the overall number of unknowns while retaining the essential features of the problem, it is assumed here that the microcrack population is distributed between sets of horizontal and vertical cracks, with respective densities defined as

$$\rho_h = N_h \langle a \rangle_h^3, \quad (2)$$

$$\rho_v = N_v \langle a \rangle_v^3, \quad (3)$$

where  $N_{h,v}$  is the number of horizontal (respectively, vertical) microcracks per unit volume of rock and  $\langle a \rangle_{h,v}$  their respective average radius. The expression for the nonzero components of  $\Delta S_{ijkl}^c$  is given in Appendix A1.

The inversion method is explained in Appendix A3. The evolution of both crack densities as a function of time was obtained by inverting the  $P$  and  $S_h$  wave speeds measured repeatedly throughout the experiments. The results of this procedure are illustrated in Figure 11, which shows the evolution of  $\rho_v$  and  $\rho_h$  as a function of axial strain during deformation, as well as the observed and modeled evolution in  $P$  and  $S_h$  wave speeds. There is a good overall agreement between the modeled and the observed wave speeds, which supports the use of the simple model outlined above and in Appendices A1 and A3.

where  $S_{ijkl}^0$  is the compliance tensor of the intact solid matrix,  $\Delta S_{ijkl}^p$  is the additional compliance due to the presence of pores, and  $\Delta S_{ijkl}^c$  is the additional compliance due to the presence of thin cracks. The additional compliance due to pores is a linear function of the volume fraction of the spherical pores in the rock; these spherical pores have the dominant contribution to the total porosity of the rock, as opposed to thin cracks. During the experiments, the porosity change is only of the order of 1% at most. Hence, the net contribution of  $\Delta S_{ijkl}^p$  to the overall compliance is mostly constant throughout the tests; in other words, it is assumed here that the dominant factor controlling the evolution in compliance (and hence in wave speed) is the growth and retraction of microcracks. The summed compliance of the intact matrix and that due to spherical pores were determined from the measured elastic wave speeds at  $P_{\text{eff}} = 50$  MPa prior to deformation, and only the change in compliance due to cracks was tracked during the deformation and recovery tests.

A general expression for  $\Delta S_{ijkl}^c$  for fluid-saturated microcracks is given in equation (A4) (see Appendix A1) as a function of one second-rank and one fourth-rank crack density tensors. In theory, all components of both these tensors are required to predict the change in compliance due to an unspecified pop-

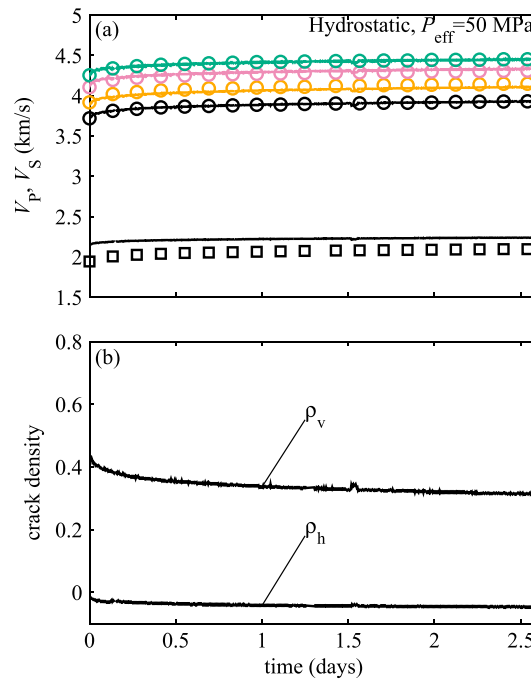


**Figure 12.** Evolution of (a) wave speeds and (b) crack densities as a function of hold time under isostatic conditions at  $P_{\text{eff}} = 50$  MPa. The crack densities  $\rho_h$  and  $\rho_v$  are defined in equations (2) and (3), respectively. Measured  $P$  wave speeds are displayed as open circles and  $S$  wave speed is shown as open squares. Modeled wave speeds are shown as continuous lines. Black, yellow, purple, and green symbols and lines correspond to  $90^\circ$  (horizontal),  $58^\circ$ ,  $39^\circ$ , and  $28^\circ$  paths, respectively.

period. Note that the starting crack density is slightly different from the one inverted during deformation due to the changes occurring during the unloading stage.

### 6.2. Crack Recovery

During deformation, the evolution of crack density results from the combined changes in both the number and the size of microcracks. However, during the static hold period it is reasonable to assume that the number of cracks per unit volume is fixed and that only the crack size and shape evolves. In the current approach, it was observed that the aspect ratio of the cracks does not significantly influence the results (see Appendix A3). Therefore, the inverted crack densities can be used to track the evolution in crack size throughout the recovery process. The relative crack recovery is computed as

$$1 - \frac{a}{a_0} = 1 - \left( \frac{\rho}{\rho_0} \right)^{1/3}, \tag{4}$$

where  $a_0$  and  $\rho_0$  are the average microcrack size and density at the beginning of the recovery process, and  $a$  and  $\rho$  are the contemporary average microcrack size and density, respectively. In equation (4), the crack size  $a$  may not strictly correspond to the actual crack size as it would be measured in the microstructure. Indeed, if contact points (“islands”) are created along the crack surface as it closes (e.g., due to local crack roughness), the crack compliance changes significantly, even though the actual crack size does not [Kachanov and Sevostianov, 2005]. Therefore, the size  $a$  as defined here from the inverted elastic wave speeds corresponds to an effective crack size, which is affected by the creation of contact points not just at the tips but all along the crack surface. In this framework, the value of  $a$  is an upper bound of the actual crack size, so the crack recovery obtained from equation (4) is also an upper bound for the actual crack retraction.

The evolution of the relative crack recovery was calculated from the inverted vertical crack density and is shown in Figure 13 for a range of test conditions. The overall relative crack recovery is of the order of 10%

During deformation, the horizontal crack density remains small and decreases slightly, so that the inverted horizontal crack density value becomes negative. The occurrence of such negative values is not surprising considering that the effective compliance prior to deformation was assumed isotropic and embedded both the contribution of the intact matrix and that of spherical pores: any preexisting isotropic microcrack distribution has thus been lumped into the initial compliance, and the inverted negative values of  $\rho_h$  simply reflect that a fraction of the preexisting initial cracks are preferentially closed when oriented perpendicular to the compression axis. In other words, the inverted crack densities correspond in fact to crack density changes from an initial isotropic crack distribution. By contrast, the vertical crack density continuously increases with increasing deformation and reaches values of the order of 0.5 to 0.6 after around 6% axial strain.

The typical behavior during recovery is illustrated in Figure 12, which shows the evolution of wave speeds and the corresponding inverted crack densities for a recovery test performed under isostatic conditions at  $P_{\text{eff}} = 50$  MPa. The horizontal crack density does not significantly change throughout the recovery period, whereas the vertical crack density decreases from around 0.44 down to 0.31 during the same

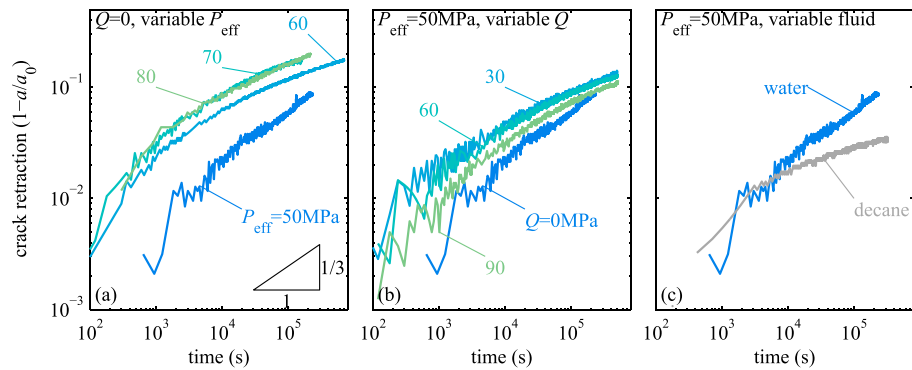


**Figure 13.** Relative microcrack recovery (computed from equation (4)) as a function of hold time for the samples deformed at  $P_{\text{eff}} = 50$  MPa until 5% axial strain and held under (a) isostatic and (b) triaxial conditions, and saturated with either (c) decane or water.

for recovery periods of the order of  $10^5$  s (i.e., 28 h). As evidenced by the log-log plots, the time evolution of microcrack recovery is not exactly matched by a power law (or an exponential law), and the recovery rate generally decreases with increasing time. A first-order estimate of the slope of the crack recovery curves yields time exponents ranging from 1/2 to 1/4 beyond the first few hundred seconds of recovery.

With increasing effective confining pressure, microcracks tend to retract somewhat faster (Figure 13a); however, this trend is probably too subtle to be significant considering the number and strength of the assumptions used in the estimates of crack recovery (in addition to the errors in the experimental measurements). Similarly, the effect of increasing differential stress while maintaining a constant  $P_{\text{eff}}$  of 50 MPa is also very modest (Figure 13b); the only visible change is to increase the rate of recovery in the first few hours of healing. By contrast, the comparison between samples held under isostatic and triaxial conditions at the same effective mean stress shows that the initial recovery rate decreases markedly with increasing differential stress (compare for instance the test performed at  $P_{\text{eff}} = 80$  MPa,  $Q = 0$  and the one at  $P_{\text{eff}} = 50$  MPa,  $Q = 90$  MPa, plotted in light green in Figures 13a and 13b, respectively). The effect of fluid type is also very significant (Figure 13c), and the recovery rate inferred for decane-saturated conditions is markedly lower than the one inferred for water-saturated conditions.

The time evolution of the vertical crack recovery was also computed for the cyclically deformed sample and is presented in Figure 14. At small strains, the estimated recovery is already quite large after the first few hundred seconds of recovery, which indicates fast initial recovery rates. With increasing strain, the initial recovery tends to be slower. The long-term evolution shows a similar qualitative pattern for all deformation steps, with the crack recovery following approximately a power law in time with exponents ranging between 1/4 and 1/3,

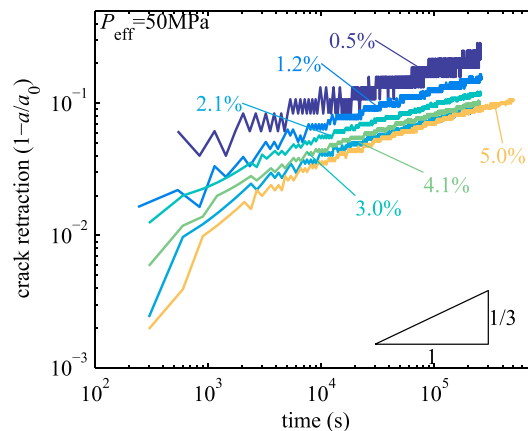


**Figure 14.** Relative microcrack recovery (computed from equation (4)) as a function of hold time for the sample deformed cyclically up to progressively larger strains (marked as percentages on the plot).

but a clear trend toward relatively slower microcrack recovery with increasing prior deformation emerges: after a  $2 \times 10^5$  s recovery period, the net relative recovery decreases from around 20% after 0.5% strain down to 0.09% after 5% strain.

## 7. Discussion: Healing Rates and Mechanisms

### 7.1. Wave Speeds Versus Permeability Change

Under all the conditions tested, a recovery in  $P$  and  $S_h$  wave speed was clearly observed during periods of constant loading after deformation; however, no concomitant changes in permeability were measured. As evidenced by the modeling results above, elastic wave speeds are very sensitive to the presence of open microcracks,

and the key parameters controlling the effect of microcracks on effective elastic moduli are scaled by a crack density which is in the form of the average microcrack volume multiplied by the number density of microcracks (see equations (2) and (3)). By contrast, permeability is controlled by a more complex combination of microcrack surface area, density, width, connectivity, and tortuosity [e.g., Guéguen and Dienes, 1989; Zhu and Wong, 1996; Kachanov and Sevostianov, 2005]. This is evident when considering that the permeability *decreases* during deformation while the crack density *increases* (Figures 2 and 11): the net decrease in permeability can be interpreted as due to the collapse of the porosity (likely both macropore and micropore, in agreement with the observed inelastic compaction) and an increase in the overall tortuosity of the fluid pathways within the rock [Zhu and Wong, 1997].

In porous rocks, a key microscale parameter controlling the permeability is the tortuosity [e.g., Zhu and Wong, 1996, 1997]. As observed in the microstructures, the microcrack network generated during deformation is very tortuous. The constant permeability measured during the healing stage of the experiments indicates that this tortuosity does not evolve significantly under the conditions and timescales of the healing tests. This interpretation implies that the inferred changes in microcrack radii (and potential changes in microcrack aperture) play only a very minor role in the overall evolution of permeability: in the porous limestone tested here, permeability evolution is dominantly driven by network parameters and not by the individual geometry of the microcracks.

### 7.2. Recovery Mechanisms in Carbonates

The observed recovery in elastic wave speeds indicates that the microcracks are retracting and closing, as discussed in section 6. The microstructural observations do show any conclusive evidence for any specific crack recovery mechanism. In this section, all the potential crack recovery mechanisms are reviewed, in an attempt to extract a subset of the most plausible mechanisms responsible for the observed recovery.

The crack recovery can be due either to mechanical closure, healing, or sealing. In the case of mechanical closure, portions of opposing microcrack faces are brought back in contact, forming bridges near the tips, but the discontinuity remains and there is no permanent reconstruction of the crystal or grain boundary structure. By contrast, for the case of crack healing or sealing, the discontinuity across the crack faces progressively disappears due to local fluxes of material, either from diffusion or precipitation [e.g., Smith and Evans, 1984; Hickman and Evans, 1987, 1992].

The occurrence of a nonnegligible elastic wave speed recovery in the absence of chemically active pore fluid (Figure 6) indicates that at least part of the recovery is due to purely mechanical closure and that this mechanical effect is time dependent. Several potential candidates can be considered for this time-dependent process: (1) local fluid flow and relaxation of pore fluid pressure, (2) creep near the microcrack tips within the fine-grained, microporous aggregates, (3) time-dependent plastic deformation (either indentation or flattening) of the particles propping the fractures open, or (4) reverse sliding on the shear cracks or defects from which wing cracks emanate. In all cases, the driving forces are the *local internal* stresses generated by the deformation; these internal stresses appear during unloading because of the interlocking of grains within the aggregate and along the microcrack faces and due to hysteresis effects arising from frictional sliding along shear cracks [e.g., Basista and Gross, 1998; David et al., 2012].

Local fluid flow is known to produce anelasticity in fluid-saturated rocks [e.g., Mavko and Nur, 1975]. Pore pressure redistribution and fluid flow after deformation may be responsible, in theory, for some crack closure and elastic wave speed recovery. However, the permeability of the samples tested here is of the order of  $10^{-16}$  m<sup>2</sup>, which implies that the characteristic hydraulic diffusion timescale across the samples is of the order of a few seconds, much shorter than the observed recovery timescale. It is therefore unlikely that pore pressure reequilibration contributes significantly to the long-term recovery.

Both creep within the fine-grained aggregate and reverse sliding on shear cracks are likely possibilities even in the decane-saturated sample, because friction is time dependent even in dry calcite [Verberne et al., 2014]: at room temperature, pure calcite and limestone aggregates show a velocity-strengthening behavior, which implies that lower slip rates tend to promote lower strengths. Hence, calcite particles and microcrack faces are expected to slide past each other at very low rates due to the residual local stresses locked-in during deformation. This microsliding is naturally expected to slow down with increasing time as the local stresses are gradually relaxed. The process of time-dependent reverse sliding on shear cracks has been evidenced in

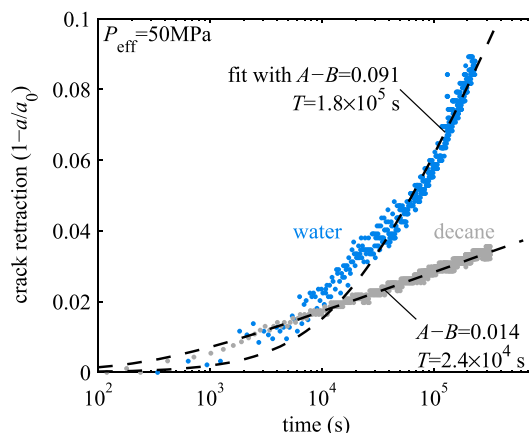


**Figure 15.** Relative microcrack recovery as a function of hold time and fits using equation (5).

depends on the elastic moduli of the rock, the applied stresses, and a characteristic frictional slip rate. The specific mathematical form of equation (5) arises from the choice of a rate-and-state friction law; it is worth noting that any other rate-strengthening friction law (or creep law) would produce a qualitatively equivalent form (although a closed form solution might not necessarily be available).

The comparison between the evolution of crack closure modeled using the wing crack geometry and those inferred from the effective medium model derived in Appendix A1 requires a note of caution. In the general wing crack geometry, the mode I “wings” are generally of complex three-dimensional shape [e.g., *Kachanov, 1982*]. Hence, the length  $\ell$  defined here in a two-dimensional model (see Appendix B) is not strictly equivalent to the microcrack radius  $a$  arising in the effective medium approach, which considers that microcracks are penny shaped. However, in practice, both  $\ell$  and  $a$  are an effective, homogenized measure of typical microcrack sizes, and their evolution in time reflects the same microscale process. Therefore, equation (5) is used here to exhibit a scaling and the main dependence of the model to the microscale parameters  $(A - B)$  and  $T$ .

Figure 15 shows two representative examples of data fits using equation (5). In the case of the decane-saturated sample held at  $P_{\text{eff}} = 50$  MPa, a very good agreement is found between the model and the data for  $(A - B) \approx 0.014$  and  $T \approx 2.4 \times 10^4$  s. Such a value for  $(A - B)$ , although relatively high compared with usual measurements for bulk rock friction (typically of the order of  $10^{-3}$ ), is still within a reasonable range. By contrast, the fit to the data from the water-saturated sample healed at  $P_{\text{eff}} = 50$  MPa requires  $(A - B) \approx 0.091$ , which is almost 1 order of magnitude higher than the value found in the decane-saturated case and is clearly out of the expected range for the rate dependence of friction in most rocks. Therefore, despite the overall decent quality of the fit in both cases, the backsliding wing crack model driven by rate-and-state friction only seems appropriate for the decane-saturated case.

The observations and the model results support the idea that the presence of free water activates specific microscale mechanisms which enhance crack closure and/or healing rates. In the low-temperature conditions of the experiments, water promotes local dissolution and precipitation processes which dramatically enhance local creep processes through pressure solution (see, for instance, *Zhang and Spiers [2005]* and *Zhang et al. [2010]*) and accelerate crack closure through both dissolution of props and precipitation of material at the crack tips [e.g., *Beeler and Hickman, 2004*]. For precipitation-driven crack healing, *Hickman and Evans [1987]* showed that the retraction of the crack tip should scale as  $t^{1/3}$  (at least at early times). This scaling is consistent with the observations in water-saturated conditions (Figure 13), even though the microstructural observations do not show direct evidence of newly precipitated material near crack tips.

One possible mechanism to explain the strong effect of water is local pressure solution of props and crack surface asperities *Beeler and Hickman [2004]*. This mechanism relies on the presence of small particles or surface roughness (e.g., due to steps formed during cleavage) along the cracks formed during the loading stage. During unloading, mismatches in crack roughness may arise due to small irrecoverable shear offset and generate asperities which prevent full closure of the microcracks. The normal stress acting on these asperities is amplified because they carry the load and also because they maintain an elastic deformation in the crack

dry granite during dilatancy recovery experiments [*Scholz and Kranz, 1974*] and therefore appears relatively universal, as it does not seem to require specific plasticity or pressure solution creep mechanisms.

By combining a simple rate-and-state friction law with a two-dimensional wing crack model, it is possible to determine the following microcrack closure law (see Appendix B):

$$1 - \frac{\ell}{\ell_0} \propto (A - B) \ln \left( 1 + \frac{t}{(A - B)T} \right), \quad (5)$$

where  $\ell$  is the length of the mode I “wings” emanating from an initial sliding shear crack,  $\ell_0$  the initial wing length,  $(A - B)$  is the rate dependency of the steady state friction coefficient,  $t$  is the time, and  $T$  is a characteristic time which

walls. The asperity contacts will tend to dissolve preferentially, allowing the crack to close and the crack tip to retract. In this situation, the crack tip retraction rate is limited by the rate at which the asperity is dissolved (or deformed). This process is overall quite similar to the backsliding mechanism described previously in that the crack tip retraction is controlled by the time-dependent closure of the central portion of the crack. Following *Beeler and Hickman* [2004], the rate of closure of a crack due to pressure-solution creep of a spherical prop is

$$\frac{dr}{dt} \approx \frac{k_+ V_m^2 s (r_0 - r)}{RT \pi (r_0^2 - (r_0 - r)^2)}, \quad (6)$$

where  $k_+$  is the dissolution rate constant,  $V_m$  is the molar volume of the material being dissolved,  $s$  is the effective stiffness of the crack,  $r_0$  is the initial radius of the prop, and  $r$  is its current radius. For  $r/r_0 \ll 1$ , equation (6) yields

$$r \approx r_0 \sqrt{t/t_c}, \quad (7)$$

where  $t_c = \pi r_0^2 RT / (k_+ s V_m^2)$  is the characteristic time of the process. If we further assume that the crack aspect ratio remains constant throughout the process, as would be expected from elastic closure, equation (7) implies that the crack retraction also scales with  $\sqrt{t}$ . This scaling is consistent, at least at early times, with the observations made in Figure 13. However, at this stage, a more detailed model accounting for the precise geometry and stress field on the crack and asperity contacts would be required to make quantitative comparisons with the data; the development of such a model is left for future studies.

### 7.3. Implications

The laboratory data on limestone presented here show a very clear recovery in seismic wave speed in the first few days following deformation episodes. In the particular conditions used in the experiments, the recovery is typically of the order of 5% of the initial wave speed after around 2 to 3 days. These experimental measurements are qualitatively consistent with seismological observations along faults following earthquakes, during which distributed deformation and damage tend to form off-fault due to the transient stress increase generated by the dynamically propagating rupture [e.g., *Andrews*, 1976, 2005].

The wave speed recovery rates inferred from seismological observations are very variable. For two earthquakes along the San Andreas fault system, *Li et al.* [2003, 2006] inferred that  $P$  and  $S$  velocities of fault zone rocks decreased by up to a few percent during the main shock, and increased by around 1% over the year following each rupture. *Schaff and Beroza* [2004] showed a similar behavior, with recoveries in  $P$  and  $S$  wave speeds of a few percent in the first few years following two different earthquakes along the San Andreas Fault system. Using a continuous seismological monitoring technique, *Brenguier et al.* [2008] showed that the surface wave speed around the San Andreas fault near Parkfield dropped by 0.06% immediately after the  $M_w$ 6.0 Parkfield earthquake and increased by a similar amount over the next 2.5 years following the main shock. Recent results using joint inversions of micro-earthquake location and velocity structure along a mid-ocean ridge transform fault [*Froment et al.*, 2014] have revealed that the  $P$  wave speed dropped by around 10% during an  $M_w$ 6.0 earthquake and recovered by up to 6% in the 20 to 30 days following the earthquake. The very wide range of inferred recovery likely results from both the variety of techniques (and their spatiotemporal resolution) and the range of tectonic context and rock types in which the faults are hosted.

Unfortunately, measurements of recovery in elastic wave speeds are not yet available for carbonate-hosted faults, so a direct quantitative comparison with the laboratory data is premature. Nevertheless, the experimental data and analysis indicate that a relatively rapid recovery can occur immediately after a loading/unloading cycle (e.g., in the damage zone after an earthquake) due to time-dependent relaxation of local stresses. This recovery is here partly due to crack closure but not necessarily associated with crack healing: indeed, elastic wave speeds are very sensitive to open microcracks and are hence dramatically affected by the formation of contact points (see discussion in *Kachanov and Sevostianov* [2005]). These contact points are very likely to form at microcrack tips or due to surface roughness of the open microcracks as the bulk of the material relaxes. Therefore, the variations in elastic properties around faults in the postseismic phase are not necessarily due to changes in macroscopic stress or to chemical healing and sealing processes but may simply arise from internal relaxation mechanisms and delayed crack closure. This internal relaxation has been shown here to be strongly dependent upon the presence of free water, which promotes local dissolution/precipitation mechanisms. Likewise, it is expected that changes in temperature and the details of the fluid chemistry will also affect the recovery rate. In nature, it is therefore expected that the recovery in seismic wave speeds around

faults does not follow a universal pattern but depends on the details of the local lithology, fluid chemistry, pressure, and temperature conditions.

## 8. Conclusions and Perspectives

It has been shown that seismic wave speeds recover significantly after deformation in the cataclastic flow regime in limestone. Under water-saturated conditions and an isostatic pressure  $P_{\text{eff}} = 50$  MPa, the typical recovery is of 5% after about 2 days. Concomitantly, the permeability remains constant, which is explained by the permanent tortuosity in the crack network generated during deformation. The recovery in wave speed has been interpreted as the result of time-dependent microcrack closure, driven by time-dependent internal friction and local pressure solution processes. The evidence for the latter were mostly inferred from the large increase in recovery rate observed in the presence of water by contrast with an inert fluid, but a direct microstructural signature remains elusive.

The recovery rates measured in the experiments on limestone are within the range of seismologically observed ones along fault immediately after earthquakes. In general, recovery of elastic wave speeds can be attributed to a range of processes, which are divided into two main classes: processes promoting crack *chemical healing or sealing*, such as surface-tension-driven healing [e.g., *Smith and Evans*, 1984], and processes promoting *mechanical closure*, which include effective stress changes (e.g., due to fluid flow) and time-dependent friction or creep. The overall recovery observed in nature is likely a combination of both types of processes, but the experimental data presented here indicate that the mechanism is likely of the second type at early times and at shallow depths, where the kinetics of chemical healing and sealing is relatively slow. Over longer timescales (several months), the recent work of *Richard et al.* [2015] has shown that thin cracks in shocked limestone are progressively healed and replaced by more spherical cavities, which indicate that dissolution-precipitation processes become gradually more significant.

Importantly, elastic wave speed recovery by crack closure does not necessarily imply a recovery in strength, since the cracks can freely reopen if stress is increased again. There is, in general, little hope that elastic wave speed recovery can be a correct proxy for strength recovery [e.g., *Kachanov and Sevostianov*, 2012] or even permeability (as demonstrated here) (see also *Kachanov and Sevostianov* [2005]). Furthermore, restrengthening is observed only when chemical healing and sealing are activated [e.g., *Tenthorey et al.*, 2003; *Tenthorey and Fitz Gerald*, 2006; *Meredith*, 2013], i.e., over much longer timescales and at higher temperatures than those tested here. Further experiments are currently being undertaken to investigate how temperature, and therefore depth in the crust, influences the rate of recovery and potentially promotes healing and sealing in addition to mechanical closure of microcracks.

## Appendix A: A Noninteractive Effective Medium Model for Cracked Porous Rocks

### A1. Elastic Compliances and Moduli

The micromechanical model used to interpret the measurements of elastic wave speed is essentially similar to that of *Fortin et al.* [2007] but includes the contribution of nonisotropically oriented cracks. The model presented here follows closely the steps presented in *Shafiro and Kachanov* [1997] and *Fortin et al.* [2007].

In the total compliance given in equation (1), the contribution of the intact material is expressed as

$$S_{ijkl}^0 = \frac{1 + \nu_0}{2E_0} (\delta_{ik}\delta_{jl} + \delta_{il}\delta_{jk}) - \frac{\nu_0}{E_0} \delta_{ij}\delta_{kl}, \quad (\text{A1})$$

where  $\nu_0$  and  $E_0$  are the Poisson's ratio and Young's modulus of the intact solid matrix, respectively, and  $\delta_{ij}$  is the Kronecker delta.

The additional compliance from fluid-saturated spherical pores is computed from the derivative of the elastic potential given in *Shafiro and Kachanov* [1997], and is expressed as

$$\Delta S_{ijkl}^p = \Phi \frac{3(1 - \nu_0)}{4E_0} \left[ \frac{10(1 + \nu_0)}{7 - 5\nu_0} (\delta_{ik}\delta_{jl} + \delta_{il}\delta_{jk}) - 2 \left( \frac{1 + 5\nu_0}{7 - 5\nu_0} + \frac{1}{3(1 + \delta_s)} \right) \delta_{ij}\delta_{kl} \right], \quad (\text{A2})$$

where  $\Phi$  is the volume fraction of spherical pores embedded in the matrix and  $\delta_s$  is a term which depends upon the bulk modulus of the fluid,  $K_f$ , as

$$\delta_s = \frac{2 E_0 / K_f - 3(1 - 2\nu_0)}{9(1 - \nu_0)}. \quad (A3)$$

The additional compliance due to fluid-saturated cracks is also found from the derivative of the elastic potential given in *Shafiro and Kachanov* [1997]:

$$\Delta S_{ijkl}^c = \frac{1}{4}(\delta_{ik}\alpha_{jl} + \delta_{il}\alpha_{jk} + \delta_{jk}\alpha_{il} + \delta_{jl}\alpha_{ik}) + \beta_{ijkl}, \quad (A4)$$

where

$$\alpha_{ij} = \frac{32(1 - \nu_0^2)}{3E_0(2 - \nu_0)} \frac{1}{V} \sum_r (a_r)^3 n_i^r n_j^r \quad (A5)$$

is the second-order crack density tensor, corresponding to a population of penny-shaped cracks of radii  $a_r$  and with normals oriented by the unit vector  $n_i^r$  within the volume  $V$ . The fourth-order crack density tensor  $\beta_{ijkl}$  is given by

$$\beta_{ijkl} = \frac{32(1 - \nu_0^2)}{3E_0(2 - \nu_0)} \frac{-2 - \nu_0\delta_c}{4(1 + \delta_c)} \frac{1}{V} \sum_r (a_r)^3 n_i^r n_j^r n_k^r n_l^r, \quad (A6)$$

where

$$\delta_c = \zeta \frac{\pi}{4(1 - \nu_0^2)} \left[ \frac{E_0}{K_f} - 3(1 - 2\nu_0) \right] \quad (A7)$$

is a factor which depends on the cracks' aspect ratio  $\zeta$  and the bulk modulus of the fluid  $K_f$ .

In the limit of a very large population of cracks, the sums in the expressions (A5) and (A6) can be replaced by integrals of the crack orientation distribution [e.g., *Hudson*, 1990]:

$$\frac{1}{V} \sum_r (a_r)^3 n_i^r n_j^r \rightarrow \frac{1}{2\pi} \int_0^{2\pi} \int_0^{\pi/2} a^3 P(\theta, \phi) n_i n_j \sin \theta d\theta d\phi, \quad (A8)$$

$$\frac{1}{V} \sum_r (a_r)^3 n_i^r n_j^r n_k^r n_l^r \rightarrow \frac{1}{2\pi} \int_0^{2\pi} \int_0^{\pi/2} a^3 P(\theta, \phi) n_i n_j n_k n_l \sin \theta d\theta d\phi, \quad (A9)$$

where  $P(\theta, \phi)$  is the number density of cracks with normal unit vectors lying in the solid angle  $(\theta, \theta+d\theta)$ ;  $(\phi, \phi+d\phi)$ , where  $\theta$  is the polar angle and  $\phi$  is the azimuthal angle. Due to the symmetry of the stress orientations during triaxial compression, the polar angle is measured from the compression axis. Hence, a crack with faces lying in the horizontal plane, perpendicular to the compression axis, has a normal oriented along  $\theta = 0$ . Conversely, vertical cracks have normals oriented along  $\theta = \pi/2$ . To proceed further, a choice must be made for the crack orientation distribution; here the microcracks are assumed to be distributed into two sets, with faces lying either in the horizontal plane (i.e., normals oriented along  $\theta = 0$ ) or in vertical planes (i.e., normals oriented along  $\theta = \pi/2$ , independently from the azimuthal angle). The resulting density function  $P$  is

$$P(\theta) = (\delta(\theta)N_h + \delta(\theta - \pi/2)N_v) / \sin \theta, \quad (A10)$$

where  $N_h$  and  $N_v$  are the number densities of horizontal and vertical cracks, respectively, and  $\delta(\cdot)$  stands for the Dirac delta. From the above density function and expressions (A8), two independent scalar crack densities can be defined; the horizontal crack density,

$$\rho_h = N_h \langle a \rangle_h^3, \quad (A11)$$

and the vertical crack density,

$$\rho_v = N_v \langle a \rangle_v^3, \quad (A12)$$

where  $\langle a \rangle_{h,v}$  is the average crack radius for the horizontal (respectively, vertical) crack population. Denoting

$$h = \frac{32(1 - \nu_0^2)}{3E_0(2 - \nu_0)}, \quad (A13)$$

$$g = \frac{32(1 - \nu_0^2)}{3E_0(2 - \nu_0)} \frac{-2 - \nu_0\delta_c}{4(1 + \delta_c)}, \quad (\text{A14})$$

the crack density tensors  $\alpha_{ij}$  and  $\beta_{ijkl}$  become

$$\alpha_{11} = \alpha_{22} = (h/2)\rho_v, \quad (\text{A15})$$

$$\alpha_{33} = h\rho_h, \quad (\text{A16})$$

$$\beta_{1111} = \beta_{2222} = (3g/8)\rho_v, \quad (\text{A17})$$

$$\beta_{3333} = g\rho_h, \quad (\text{A18})$$

$$\beta_{1122} = \beta_{2211} = \beta_{1212} = \beta_{2121} = (g/8)\rho_v, \quad (\text{A19})$$

all other components being zero. The resulting additional elastic compliance due to cracks is hence given by

$$\Delta S_{1111}^c = \Delta S_{2222}^c = (h/2 + 3g/8)\rho_v, \quad (\text{A20})$$

$$\Delta S_{3333}^c = (h + g)\rho_h, \quad (\text{A21})$$

$$\Delta S_{1212}^c = (h/4 + g/8)\rho_v, \quad (\text{A22})$$

$$\Delta S_{1313}^c = \Delta S_{2323}^c = (h/4)(\rho_v/2 + \rho_h), \quad (\text{A23})$$

$$\Delta S_{1122}^c = (g/8)\rho_v, \quad (\text{A24})$$

all other components being zero.

By inverting the compliance tensor resulting from the summation of each contribution, the stiffness tensor is obtained and reads (in Voight's notation):

$$C_{11} + C_{22} = \left[ S_{11}^{0,p} + (h + g)\rho_h \right] / D, \quad (\text{A25})$$

$$C_{11} - C_{22} = \left[ S_{11}^{0,p} - S_{12}^{0,p} + (h/2 + g/4)\rho_v \right]^{-1}, \quad (\text{A26})$$

$$C_{33} = \left[ S_{11}^{0,p} + S_{12}^{0,p} + (h/2 + g/2)\rho_v \right] / D, \quad (\text{A27})$$

$$C_{44} = \left[ 2S_{11}^{0,p} - 2S_{12}^{0,p} + h(\rho_v/2 + \rho_h) \right]^{-1}, \quad (\text{A28})$$

$$C_{13} = -S_{12}^{0,p} / D, \quad (\text{A29})$$

$$C_{66} = \left[ 2S_{11}^{0,p} - 2S_{12}^{0,p} + (h + g/2)\rho_v \right]^{-1}, \quad (\text{A30})$$

where

$$D = \left[ S_{11}^{0,p} + (h + g)\rho_h \right] \left[ S_{11}^{0,p} + S_{12}^{0,p} + (h/2 + g/2)\rho_v \right] - 2(S_{12}^{0,p})^2. \quad (\text{A31})$$

The compliances  $S_{11}^{0,p}$  and  $S_{12}^{0,p}$  correspond to the two independent components obtained from the sum of the compliances of the intact material and that due to spherical pores (both contributions having the same symmetries).

### A2. Wave Speeds

The elastic wave speed along a propagation angle  $\vartheta$  measured from the compression axis of the sample are computed from the effective stiffness tensor and the density of the rock  $\rho_{\text{rock}}$  as

$$V_p(\vartheta) = \left[ \left( C_{11} \sin^2 \vartheta + C_{33} \cos^2 \vartheta + C_{44} + \sqrt{M} \right) / (2\rho_{\text{rock}}) \right]^{1/2}, \quad (\text{A32})$$

$$V_{sh}(\vartheta) = \left( C_{66} \sin^2 \vartheta + C_{44} \cos^2 \vartheta \right)^{1/2} / \rho \quad (\text{A33})$$

where

$$M = \left[ (C_{11} - C_{44}) \sin^2 \vartheta - (C_{33} - C_{44}) \cos^2 \vartheta \right]^2 + [(C_{13} + C_{44}) \sin 2\vartheta]^2. \quad (\text{A34})$$

### A3. Inversion Procedure

The inversion method is similar to the one used in *Brantut et al.* [2011] and is based on the general theory of *Tarantola* [2005]. In the model outlined in Appendix A1, four parameters are required to compute the elastic compliances (and hence the wave speeds): the two crack densities  $\rho_v$  and  $\rho_h$ , the microcracks aspect ratio  $\zeta$ , and the porosity due to spherical pores  $\Phi$ .

Because of the noninteraction hypothesis, the superposition principle holds and one can bypass the need to constrain accurately the effect of pores (and any isotropic distribution of microcracks) by simply assuming that the measured compliances of the rock prior to deformation (i.e., while the material is still isotropic) corresponds to  $S_{11}^{0,p}$  and  $S_{12}^{0,p}$ . The overall porosity of the rock only changes modestly during deformation and healing, and the effect of spherical pores on the effective compliance is small compared to that of thin cracks; it is then assumed that  $S_{11}^{0,p}$  and  $S_{12}^{0,p}$  remain approximately constant throughout the experiments. Therefore, the parameter  $\Phi$  is not explicitly required for the computation of the total effective elastic properties of the rock. Based on the average wave speeds measured at  $P_{\text{eff}} = 50$  MPa prior to deformation, effective compliances of  $S_{11}^{0,p} = 1/40$  GPa<sup>-1</sup> and  $S_{12}^{0,p} = -0.28/40$  GPa<sup>-1</sup> were determined.

The microcrack aspect ratio  $\zeta$  is assumed here to be zero, which is equivalent to assuming that the cracks are constrained against opening [*Kachanov*, 1993, p. 382]. Inversion tests were performed without constraining  $\zeta = 0$  and confirmed that the overall impact on the inverted crack densities was negligible. Therefore, only two unconstrained parameters,  $\rho_v$  and  $\rho_h$ , need to be inverted.

The elastic moduli of the intact solid skeleton, required to compute the constants  $h$  and  $g$  (see equations (A13) and (A14)), were calculated from the Voight-Reuss-Hill averages for a mixture of 80% calcite and 20% quartz. The corresponding Young's modulus is  $E_0 = 78.6$  GPa and the Poisson's ratio is  $\nu_0 = 0.29$ .

In the inverse problem formulation, the data correspond to the measurements of  $V_p$  along the four available orientations ( $\vartheta = 90^\circ, 58^\circ, 39^\circ$ , and  $28^\circ$ ) and  $V_{sh}$  along the horizontal direction. The associated measurement errors were assumed to follow a Laplace distribution with a scale parameter (i.e., the measurement error) of 100 m/s. The model parameters, as discussed above, are the two crack densities  $\rho_v$  and  $\rho_h$ . The parameter space is only two dimensional and was hence explored entirely. The result of the inversion is a probability density function over the  $(\rho_v, \rho_h)$  space, and the "best" solution was chosen following the least absolute value criterion.

## Appendix B: The Backsliding Wing Crack Model

A very common microphysical approach to model the deformation of brittle materials is to assume that the material is a linear elastic solid which contains a set of preexisting cracks or flaws. When subjected to compressive loads, the preexisting cracks tend to slide and generate open mode I "wing cracks" oriented parallel to the maximum compressive stress [e.g., *Brace and Bombolakis*, 1963; *Kachanov*, 1982; *Nemat-Nasser and Hori*, 1982]. During unloading, the shear cracks tend to slide in the reverse direction and the wing cracks tend to mechanically close. Here we analyze how this reverse sliding and closure mechanism can extend over time after unloading, under constant stress conditions, due to time-dependent variations in the frictional properties of the sliding cracks.

Although wing crack models have been extensively developed and used to analyze deformation and failure of rocks [see *Paterson and Wong*, 2005, chapter 6], a relatively small number of studies have focused on the behavior of cracked rocks during unloading. In the spirit of making elementary estimates and develop simple

scalings, we will use here the two-dimensional model given by *Basista and Gross* [1998], which has the benefit of devoting some attention to the unloading behavior. In this model, the wing crack geometry is based on initial flaws of length  $2c$  oriented at an angle  $\psi$  to the maximum compressive stress, which develop straight wings of length  $\ell$ , oriented parallel to the maximum compressive stress.

The slip displacement  $b$  on the initial flaw induced by the applied stresses is given by [*Basista and Gross*, 1998]

$$b = \frac{4(1 - \nu^2)}{E} (\tau_{\text{eff}}c - \sigma_2 \cos \psi \ell), \quad (\text{B1})$$

where  $\nu$  is the Poisson's ratio and  $E$  is the Young's modulus of the matrix,  $\sigma_2$  is the applied lateral (confining) stress, and  $\tau_{\text{eff}}$  is the effective shear stress on the initial flaw. This effective stress is the difference between the resolved shear stress on the flaw,  $\tau$ , and the resisting frictional shear stress  $\mu\sigma_n$ ,

$$\tau_{\text{eff}} = \tau \pm \mu\sigma_n \quad (\text{B2})$$

where,  $\mu$  is the friction coefficient and  $\sigma_n$  is the resolved normal stress on the flaw. Compressive stresses are taken positive; in equation (B2), the minus sign is used upon forward sliding ( $\tau \geq 0$ ) and the plus sign is used upon reverse sliding ( $\tau \leq 0$ ).

Note that equation (B1) applies only when the condition for the onset of sliding (or backsliding) is satisfied. In the case of unloading, this condition is expressed by *Basista and Gross* [1998] from the peak elastic restoring forces associated with the opening of the wing cracks at the end of the loading phase. The knowledge of these elastic restoring forces requires a detailed modeling of the full loading history; here for the sake of simplicity we will assume that the backsliding condition is satisfied at least at the end of the unloading stage, where the differential stress becomes zero while the confining pressure remains constant.

Differentiation of equation (B1) with respect to time, assuming constant isostatic stress ( $\tau = 0$ ,  $\sigma_n = \sigma_2 > 0$ ) leads to the following expression for the increment in reverse slip:

$$\frac{db}{dt} = \frac{4(1 - \nu^2)}{E} \left( \sigma_n c \frac{d\mu}{dt} - \sigma_2 \cos \psi \frac{d\ell}{dt} \right), \quad (\text{B3})$$

The closure condition for the wing cracks is given by equating the mode I stress intensity factor at the crack tips to zero,  $K_I = 0$ . The expression for  $K_I$  is [*Basista and Gross*, 1998]

$$K_I = \sqrt{c} 2\pi \left[ \frac{E}{2(1 - \nu^2)} \frac{b}{\sqrt{\ell}} \cos \psi - \pi \sigma_2 \sqrt{\ell} \right], \quad (\text{B4})$$

and hence the wing crack closure condition is

$$\frac{E}{2(1 - \nu^2)} b \cos \psi - \pi \sigma_2 \ell = 0. \quad (\text{B5})$$

The condition for continuous closure through time is then  $dK_I/dt = 0$ , which yields (assuming constant stresses)

$$\frac{E}{2(1 - \nu^2)} \cos \psi \frac{db}{dt} - \left[ \frac{E}{2(1 - \nu^2)} \cos \psi \frac{b}{2\ell} + \pi \sigma_2 \right] \frac{d\ell}{dt} = 0. \quad (\text{B6})$$

Finally, the coefficient of friction  $\mu$  is expressed as a function of the reverse sliding velocity  $db/dt$  by using the steady state form of the rate-and-state friction law [e.g., *Dieterich*, 1979; *Ruina*, 1983]:

$$\mu = \mu_0 + (A - B) \ln \left( (1/V_0) |db/dt| \right), \quad (\text{B7})$$

where  $\mu_0$  is a reference (constant) friction coefficient,  $(A - B)$  is the steady state rate dependence of friction, assumed positive for calcite, and  $V_0$  a reference speed. Reorganizing, we obtain a differential equation for the backsliding rate

$$\frac{db}{dt} = -V_0 \exp \left( \frac{\mu - \mu_0}{A - B} \right), \quad (\text{B8})$$

where the minus sign ensures that the total slip  $b$  is indeed decreasing over time.

The crack closure condition (B5) implies that the ratio  $b/\ell$  remains constant throughout the backsliding process. The combination of equations (B3), (B6), and (B8) can thus be solved analytically for  $b(t)$ ,  $\mu(t)$ , and  $\ell(t)$ . The result for the wing crack length is

$$\ell(t) = \ell_0 - c \frac{\cos \psi}{\pi/2 + \cos^2 \psi} (A - B) \ln \left( 1 + \frac{t}{(A - B)T} \right), \quad (\text{B9})$$

where the equality  $\sigma_n = \sigma_2$  was used and where  $\ell_0$  is the initial wing crack length at  $t = 0$ . In equation (B9),  $T$  is a characteristic time given by

$$T = \frac{c}{V_0} \frac{2\pi\sigma_n(1 - \nu^2)}{(\pi/2 + \cos^2 \psi)E}. \quad (\text{B10})$$

#### Acknowledgments

This work was supported by the UK Natural Environment Research Council through grant NE/K009656/1. The data from this paper are available from the author upon request. I thank Tom Mitchell for useful discussions and Phil Meredith for a thorough review of an earlier version of the manuscript. I am thankful to an anonymous reviewer and to Brian Evans for their comments, which improved the paper significantly.

#### References

- Andrews, D. J. (1976), Rupture propagation with finite stress in antiplane strain, *J. Geophys. Res.*, *81*(20), 3575–3582.
- Andrews, D. J. (2005), Rupture dynamics with energy loss outside the slip zone, *J. Geophys. Res.*, *110*, B01307, doi:10.1029/2004JB003191.
- Basista, M., and D. Gross (1998), The sliding crack model of brittle deformation: An internal variable approach, *Int. J. Solids Struct.*, *35*(5–6), 487–509.
- Beeler, N. M., and S. H. Hickman (2004), Stress-induced, time-dependent fracture closure at hydrothermal conditions, *J. Geophys. Res.*, *109*, B02211, doi:10.1029/2002JB001782.
- Bernabé, Y., U. Mok, and B. Evans (2006), A note on the oscillating flow method for measuring rock permeability, *Int. J. Rock Mech. Min. Sci.*, *43*(2), 311–316.
- Brace, W. F., and E. G. Bombolakis (1963), A note on brittle crack growth in compression, *J. Geophys. Res.*, *68*(12), 3709–3713.
- Brantley, S. L. (1992), The effect of fluid chemistry on quartz microcrack lifetimes, *Earth Planet. Sci. Lett.*, *113*, 145–156.
- Brantley, S. L., B. Evans, S. H. Hickman, and D. A. Crerar (1990), Healing of microcracks in quartz: Implications for fluid flow, *Geology*, *18*, 136–139.
- Brantut, N., A. Schubnel, and Y. Guéguen (2011), Damage and rupture dynamics at the brittle-ductile transition: The case of gypsum, *J. Geophys. Res.*, *116*, B01404, doi:10.1029/2010JB007675.
- Brantut, N., M. J. Heap, P. Baud, and P. G. Meredith (2014a), Rate- and strain-dependent brittle deformation of rocks, *J. Geophys. Res. Solid Earth*, *119*, 1818–1836, doi:10.1002/2013JB010448.
- Brantut, N., M. J. Heap, P. Baud, and P. G. Meredith (2014b), Mechanisms of time-dependent deformation in porous limestone, *J. Geophys. Res. Solid Earth*, *119*, 5444–5463, doi:10.1002/2014JB011186.
- Brenguier, F., M. Campillo, C. Hadziioannou, N. M. Shapiro, R. M. Nadeau, and E. Larose (2008), Postseismic relaxation along the San Andreas fault at Parkfield from continuous seismological observations, *Science*, *321*, 1478–1481.
- Budiansky, B., and R. J. O'Connell (1976), Elastic moduli of a cracked solid, *Int. J. Solids Struct.*, *12*, 81–97.
- David, E. C., N. Brantut, A. Schubnel, and R. W. Zimmerman (2012), Sliding crack model for nonlinearity and hysteresis in the uniaxial stress-strain curve of rock, *Int. J. Rock Mech. Min. Sci.*, *52*, 9–17.
- Dieterich, J. H. (1979), Modeling of rock friction 1. Experimental results and constitutive equations, *J. Geophys. Res.*, *84*(B5), 2161–2168.
- Eccles, D., P. R. Sammonds, and O. C. Clint (2005), Laboratory studies of electrical potential during rock fracture, *Int. J. Rock Mech. Min. Sci.*, *42*(7–8), 933–949.
- Faulkner, D. R., T. M. Mitchell, D. Healy, and M. J. Heap (2006), Slip on 'weak' faults by the rotation of regional stress in the fracture damage zone, *Nature*, *444*, 922–925, doi:10.1038/nature05353.
- Faulkner, D. R., C. A. L. Jackson, R. J. Lunn, R. W. Schlichte, Z. K. Shipton, C. A. J. Wibberley, and M. O. Withjack (2010), A review of recent developments concerning the structure, mechanics and fluid flow properties of fault zones, *J. Struct. Geol.*, *32*, 1557–1575.
- Fischer, G. J., and M. S. Paterson (1992), Measurement of permeability and storage capacity in rocks during deformation at high temperature and pressure, in *Fault Mechanics and Transport Properties of Rocks*, *Int. Geophys. Ser.*, edited by B. Evans and T. F. Wong, pp. 187–211, Academic Press, London.
- Fortin, J., Y. Guéguen, and A. Schubnel (2007), Effects of pore collapse and grain crushing on ultrasonic velocities and  $v_p/v_s$ , *J. Geophys. Res.*, *112*, B08207, doi:10.1029/2005JB004005.
- Froment, B., J. J. McGuire, R. D. van der Hilst, P. Gouédard, E. C. Roland, H. Zhang, and J. A. Collins (2014), Imaging along-strike variations in mechanical properties of the Gofar transform fault, East Pacific Rise, *J. Geophys. Res. Solid Earth*, *119*, 7175–7194, doi:10.1002/2014JB011270.
- Gratier, J.-P., D. K. Dysthe, and F. Renard (2013), The role of pressure solution creep in the ductility of the Earth's upper crust, in *Advances in Geophysics*, vol. 54, edited by R. Dmowska, pp. 47–179, Elsevier, San Diego, Calif.
- Guéguen, Y., and J. Dienes (1989), Transport properties of rocks from statistics and percolation, *Math. Geol.*, *21*(1), 1–13.
- Guéguen, Y., and M. Kachanov (2011), Effective elastic properties of cracked and porous rocks—An overview, in *Mechanics of Crustal Rocks*, edited by Y. M. Leroy and F. K. Lehner, pp. 73–125, Springer, Berlin.
- Hickman, S. H., and B. Evans (1987), Influence of geometry upon crack healing rate in calcite, *Phys. Chem. Miner.*, *15*, 91–102.
- Hickman, S. H., and B. Evans (1992), Implications for diagenesis, lithification and strength recovery, in *Fault Mechanics and Transport Properties of Rocks*, *Int. Geophys. Ser.*, edited by B. Evans and T. F. Wong, pp. 187–211, Academic Press, London.
- Huang, Y., J.-P. Ampuero, and D. V. Helmberger (2014), Earthquake ruptures modulated by waves in damaged fault zones, *J. Geophys. Res. Solid Earth*, *119*, 3133–3154, doi:10.1002/2013JB010724.
- Hudson, J. A. (1990), Overall elastic properties of isotropic materials with arbitrary distribution of circular cracks, *Geophys. J. Int.*, *102*, 465–469.
- Jaeger, J. C., N. G. W. Cook, and R. W. Zimmerman (2007), *Fundamentals of Rock Mechanics*, 4th ed., Blackwell, Oxford, U. K.
- Kachanov, M. (1993), Elastic solids with many cracks and related problems, in *Advances in Applied Mechanics*, vol. 30, edited by J. W. Hutchinson and T. Y. Wu, pp. 259–445, Academic Press, New York, doi:10.1016/S0065-2156(08)70176-5.
- Kachanov, M., and I. Sevostianov (2005), On quantitative characterization of microstructures and affective properties, *Int. J. Solids Struct.*, *42*, 309–336.

- Kachanov, M., and I. Sevostianov (2012), Rice's internal variables formalism and its implications for the elastic and conductive properties of cracked materials, and for the attempts to relate strength to stiffness, *J. Appl. Mech.*, *79*(3), 031002, doi:10.1115/1.4005957.
- Kachanov, M. L. (1982), A microcrack model of rock inelasticity. Part II: Propagation of microcracks, *Mech. Mater.*, *1*, 29–41.
- Kaproph, B. M., and C. Marone (2014), Evolution of elastic wave speed during shear-induced damage and healing within laboratory fault zones, *J. Geophys. Res. Solid Earth*, *119*, 4821–4840, doi:10.1002/2014JB011051.
- Karner, S. L., C. Marone, and B. Evans (1997), Laboratory study of fault healing and lithification in simulated fault gouge under hydrothermal conditions, *Tectonophysics*, *277*, 41–55.
- Li, Y.-G., J. E. Vidale, S. M. Day, D. D. Oglesby, and E. Cochran (2003), Postseismic fault healing on the rupture zone of the 1999 *M* 7.1 Hector Mine, California, earthquake, *Bull. Seismol. Soc. Am.*, *93*(2), 854–869.
- Li, Y.-G., P. Chen, E. S. Cochran, J. E. Vidale, and T. Burdette (2006), Seismic evidence for rock damage and healing on the San Andreas fault associated with the 2004 *M* 6.0 Parkfield earthquake, *Bull. Seismol. Soc. Am.*, *96*(4B), S349–S363.
- Mavko, G., and A. Nur (1975), Melt squirt in the asthenosphere, *J. Geophys. Res.*, *80*(11), 1444–1448.
- Meredith, P. G. (2013), Strength recovery and vein growth during self-sealing of experimentally-induced faults in westerly granite, Abstract MR41B–08 presented at 2013 Fall Meeting, AGU, San Francisco, Calif., 9–13 Dec.
- Mitchell, T. M., and D. R. Faulkner (2008), Experimental measurements of permeability evolution during triaxial compression of initially intact crystalline rocks and implications for fluid flow in fault zones, *J. Geophys. Res.*, *113*, B11412, doi:10.1029/2008JB005588.
- Morrow, C. A., D. E. Moore, and D. A. Lockner (2001), Permeability reduction in granite under hydrothermal conditions, *J. Geophys. Res.*, *106*(B12), 30,551–30,560.
- Nakatani, M., and C. H. Scholz (2004), Frictional healing of quartz gouge under hydrothermal conditions: 1. Experimental evidence for solution transfer healing mechanism, *J. Geophys. Res.*, *109*, B07201, doi:10.1029/2001JB001522.
- Nemat-Nasser, S., and H. Horii (1982), Compression-induced nonplanar crack extension with application to splitting, exfoliation, and rockburst, *J. Geophys. Res.*, *87*(B8), 6805–6821.
- Paterson, M. S., and T. F. Wong (2005), *Experimental Rock Deformation—The Brittle Field*, 2nd ed., Springer, Berlin.
- Rempe, M., T. M. Mitchell, J. Renner, S. Nippres, Y. Ben-Zion, and T. Rockwell (2013), Damage and seismic velocity structure of pulverized rocks near the San Andreas fault, *J. Geophys. Res. Solid Earth*, *118*, 2813–2831, doi:10.1002/jgrb.50184.
- Richard, J., M.-L. Doan, J.-P. Gratier, and F. Renard (2015), Microstructures induced in porous limestone by dynamic loading, and fracture healing: An experimental approach, *Pure Appl. Geophys.*, *172*, 1269–1290.
- Ruina, A. L. (1983), Slip instability and state variable friction laws, *J. Geophys. Res.*, *88*, 10,359–10,370.
- Rutter, E. H. (1976), The kinetics of rock deformation by pressure solution, *Philos. Trans. R. Soc. A*, *283*(1312), 203–219.
- Salganik, R. L. (1973), Mechanics of bodies with many cracks, *Mech. Solids*, *8*(4), 135–143.
- Sayers, C., and M. Kachanov (1995), Microcrack-induced elastic wave anisotropy of brittle rocks, *J. Geophys. Res.*, *100*(B3), 4149–4156.
- Schaff, D. P., and G. C. Beroza (2004), Coseismic and postseismic velocity changes measured by repeating earthquakes, *J. Geophys. Res.*, *109*, B10302, doi:10.1029/2004JB003011.
- Scholz, C. H. (2002), *The Mechanics of Earthquake and Faulting*, 2nd ed., Cambridge Univ. Press, Cambridge, U. K.
- Scholz, C. H., and R. L. Kranz (1974), Notes on dilatancy recovery, *J. Geophys. Res.*, *79*(14), 2132–2135.
- Schubnel, A., J. Fortin, L. Burlini, and Y. Guéguen (2005), Damage and recovery of calcite rocks deformed in the cataclastic regime, in *High-Strain Zones: Structure and Physical Properties*, edited by D. Bruhn and L. Burlini, *Geol. Soc. London Spec. Publ.*, *245*, 203–221.
- Shafiro, B., and M. Kachanov (1997), Materials with fluid-filled pores of various shapes: Effective elastic properties and fluid pressure polarization, *Int. J. Solids Struct.*, *34*(27), 3517–3540.
- Smith, D. L., and B. Evans (1984), Diffusional crack healing in quartz, *J. Geophys. Res.*, *89*(B6), 4125–4135.
- Tarantola, A. (2005), *Inverse Problem Theory*, 2nd ed., Soc. for Ind. Math., Philadelphia.
- Tenthorey, E., and J. D. Fitz Gerald (2006), Feedbacks between deformation, hydrothermal reaction and permeability evolution in the crust: Experimental insights, *Earth Planet. Sci. Lett.*, *247*, 117–129.
- Tenthorey, E., C. H. Scholz, and E. Aharonov (1998), Precipitation sealing and diagenesis: 1. Experimental results, *J. Geophys. Res.*, *103*(B10), 23,951–23,967.
- Tenthorey, E., S. F. Cox, and H. F. Todd (2003), Evolution of strength recovery and permeability during fluid-rock reaction in experimental fault zones, *Earth Planet. Sci. Lett.*, *206*, 161–172.
- Verberne, B. A., C. J. Spiers, A. R. Niemeijer, J. H. P. De Bresser, D. A. M. De Winter, and O. Plümpner (2014), Frictional properties and microstructure of calcite-rich fault gouges sheared at sub-seismic velocities, *Pure Appl. Geophys.*, *171*, 2617–2640.
- Wong, T.-F., and P. Baud (2012), The brittle-ductile transition in porous rock: A review, *J. Struct. Geol.*, *44*, 25–53.
- Zhang, X., and C. J. Spiers (2005), Compaction of granular calcite by pressure solution at room temperature and effects of pore fluid chemistry, *Int. J. Rock Mech. Min. Sci.*, *42*, 950–960.
- Zhang, X., C. J. Spiers, and C. J. Peach (2010), Compaction creep of wet granular calcite by pressure solution at 28°C to 150°C, *J. Geophys. Res.*, *115*, B09217, doi:10.1029/2008JB005853.
- Zhu, W., and T.-F. Wong (1996), Permeability reduction in a dilating rock: Network modeling of damage and tortuosity, *Geophys. Res. Lett.*, *23*(22), 3099–3102.
- Zhu, W., and T.-F. Wong (1997), The transition from brittle faulting to cataclastic flow: Permeability evolution, *J. Geophys. Res.*, *102*(B2), 3027–3041.
- Zimmerman, R. W. (1991), *Compressibility of Sandstones*, Elsevier, Amsterdam.